Article:

Ghadbeigi, H., Yu, F., Pinna, C. et al. (2025) Failure analysis of resistance spot welds in a DP1000 automotive steel: full field macro/ micro scale deformation analysis. Journal of Design Against Fatigue, 3 (2). pp. 1-17. ISSN: 2976-940X

https://doi.org/10.62676/jdaf.2025.3.2.10

Journal of Design Against Fatigue, Vol. 3, No.2 (2025) 1-17

Journal of Design Against Fatigue
https://minerva-aset.com/JDAF
MINERVA ASET
ISSN 2976-940X

Failure analysis of resistance spot welds in a DP1000 automotive steel: full field macro/ micro scale deformation analysis

H. Ghadbeigi*[a], F. Yu[a], C. Pinna[a], S. Smith[b], E. van der Aa[c]
[a] *School of Mechanical, Aerospace and Civil Engineering, The University of Sheffield, Sheffield, UK*
[b] *National Structural Integrity Centre, The Welding Institute, Cambridge, UK*
[c] *Tata Steel R&D, IJmuiden, The Netherlands*

PAPER INFO

Paper history:
Received 17 August 2025
Received in revised form 11 September 2025
Accepted 13 September 2025

Keywords:
Keywords:
Resistance Spot Weld
DP1000
Fracture
Strain distribution
Digital Image Correlation

ABSTRACT

The effect of welding parameters on local deformation and failure of resistance spot welds in a DP1000 high strength dual phase steel are investigated. A novel experimental framework is developed together with new sample geometries to investigate failure modes in the weld sections. Macro and microscopic experiments using optical and scanning electron imaging combined with digital image correlation are used to better understand the role of microstructural morphology and loading conditions on deformation and damage of the weld nugget in the studied materials. The results show a transition from the interfacial failure to pull-out failure as the welding current increases. The measured plastic strain at failure is larger for higher welding currents. The fracture surface at the nugget is dominated by brittle and shear fracture for interfacial failure mode in samples produced with lower welding current, however ductile and shear fracture are more pronounced on the samples with pull-out failure mode under higher welding current.

https://doi.org/10.62676/jdaf.2025.3.2.10

1. INTRODUCTION

Advanced high strength steels (AHSS) have been widely used as part of body-in-white in the automotive industry. The ductility-strength combination of the materials is extremely attractive as thinner gauge dimensions could deliver the required functional performance of the structures. Dual phase steels are a grade of AHSS wherein the materials show a continuous yielding behaviour with an extended plasticity at a strength of as high as 1000[1] . Resistance spot welding (RSW) is the preferred technique to join steel structures and panels during assembly of body-in-whites and a certain level of structural performance in accidents and crash loading is expected from the produced welds loading. As the materials experiences a localised melting and heat treatment during the RSW process, the higher content of alloying elements in DP steels may result in an unexpected mechanical failure in the welded structures. This is partially because different microstructural morphologies could be formed in the spot welds after cooling affecting the functional performance and strength. These include base metal (BM), heat affected zone (HAZ) and the nugget [1]. There are several failure modes reported for the resistance spot welds [2-4], including pull-out failure (PF), partial interfacial failure (PIF) and interfacial failure (IF). Postmortem analysis of the fractured welds indicated that the former involves a failure initiation from an interfacial notch tip, where the two sheets are forged due to the applied current and force, and propagates through the thickness direction, inside HAZ or in BM near the interface between BM and HAZ, leading to the catastrophic failure [5,6]. This is the most preferred failure mode as large amount of mechanical energy is consumed during plastic deformation in the weld and the HAZ/BM reduces the impact energy transferred to main structures. It is reported that the main

---

*Corresponding Author Email: *h.ghadbeigi@sheffield.ac.uk* (Hassan Ghadbeigi)

Cite this article as: H.Ghadbeigi, F. Yu, C. Pinna, S. Smith , E. van der Aa , Failure analysis of resistance spot welds in a DP1000 automotive steel: full field macro/ micro scale deformation analysis, ***Journal of Design Against Fatigue,*** Vol. 3, No. 2, (2025), 1-17
https://doi.org/10.62676/jdaf.2025.3.2.10

mechanism of partial interfacial failure (PIF) and interfacial failure (IF) is linked to cracks propagating directly into the nugget that results in the least failure energy absorption [3,5]. The observed mode of fracture is directly linked to the applied welding parameters including current, dwell time and pressure [7]. Standard test geometries such as Tensile Shear (TS) [5,8], Coach-Peel (CP) [5] and Cross-Tension (CT) [1,9] have already been used to investigate fracture and failure mechanisms of automotive steels and the associated effect of materials microstructure. Failure mechanisms of welded CT samples in DP450 and DP980, with same welding parameters, were investigated by Dancette et al. [1]. They showed DP450 steel samples failed via PF mode caused by ductile fracture while DP980 failed through PIF mode caused by semi-brittle fracture. Additionally, it is also reported that increasing the welding current results in enlarged nugget that promotes a failure mode transition from PIF or PF to PF of CT sample in DP590 [5]. Different failure mechanisms are reported for identical TS sample geometries made from DP980 [3,10] and DP600 [11] automotive steels. The authors reported that DP980 samples failed by shear fracture, while combined shear-ductile fracture was observed in the fracture surface of DP600 samples with ductile voids located at the circumference of the nugget. Despite the scarcity of knowledge about failure of AHSS in the coach-peel test conditions, bending induced stresses are reported to lead to ductile and shear dominant pull-out failure in a low carbon steel while notch tip blunting and ductile fracture derive PF mode in welds of a grade of HSLA steel [7]. Postmortem analysis of the fracture surfaces of the weld section was the focus of most reports on spot weld failure that could reveal a correlation between the applied welding parameters and the failure mode. However, no insight into the deformation state of the material within different weld zones has been provided. To the best knowledge of the authors, there is little knowledge of the local deformation mechanics in the weld section linked to the deformation and failure mechanisms as well as microstructural morphologies of the weld for the advanced automotive steels and specifically for high strength AHSS .

Different full field strain measurement techniques, such as grid method, moiré interferometry and digital image correlation (DIC), have already been implemented to measure local and full field strain distribution at micro or macro scales [12-15]. Among these, DIC has been widely applied to study the deformation and damage evolution at different length scales due to the versatility of the image analysis techniques developed in the past decades and it has been proved to be a reliable tool to determine in-plane and out of plane deformation as reported in [13,16,17]. It has already been shown that Scanning Electron Microscopy images together with the DIC technique can be used to determine damage and failure mechanisms linked to measure local deformation at the scale of microstructure [18]. Siebert et al. [19] found that maximum error strain measured by DIC is only around 5% comparing to strain gauge according to standard tensile test. To achieve accurate measurements using DIC, illumination, calibration, quality of speckle patterns and the right selection of subset size are needed to be considered [20,21].

Traditional hardness-scaling methods often fail to capture true stress-strain behaviour across weld zones. Midawi et al. [22] present a novel DIC-enhanced approach using sub-size tensile and mini-shear tests for accurate local constitutive data. There are already some reports [23-27] on the application of DIC to determine mechanical properties of various regions in RSW using conventional shear tests or half-cut tensile samples at macro-scale [27,28]. However, these do not indicate the role of different microstructural regions during the fracture .

In the present research the effects of welding current and contribution of different microstructural zones within the weld sections on the deformation and failure mechanisms of the weld nugget of a DP1000 advanced automotive steel were studied. In this context, new sample geometries were developed and in-situ optical and scanning electron microscopy-based experiments combined with Stereo DIC technique were used to measure local, macro and micro scale, plastic deformation across the weld sections, for the first time. The measured multi-scale deformation distribution is linked to the applied welding currents and observed failure modes to enhance the understanding of the failure mechanisms in the weld that is required for the development of predictive models of failure.

2. METHODOLOGY

2.1 Design of New Sample Geometries

A dual phase steel (DP1000) with a sheet thickness of 1.2mm and the given microstructural morphology of Figure **1** was used in this study. **Table 1** shows the tensile mechanical properties of the as received material [29]. New sample geometries, Macro CP, Micro CP (MiCP) and modified TS samples, were designed to enable in-situ quantitative measurement of the local deformation fields and to investigate failure development within the weld nuggets subjected to different loading conditions [5,8,30,31]. Standard tensile shear (TS) geometries as described in [5,32] were modified to design the new geometries. A double weld setup was used followed by sectioning the samples across the weld nuggets and mechanical polishing as it is shown in Figure **2**. The samples were prepared in such a way that each side of the section contains a half-weld and loaded symmetrically and hence experiencing identical stress state, after cutting and preparation. A Finite Element (FE) parametric study was carried out in Abaqus/Explicit package in order to determine the optimum dimensions for the designed geometries and the welding pitch to satisfy the stress state for the required failure modes.

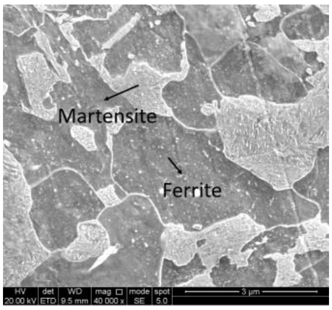

Figure 1. Microstructure of the DP1000 sheet showing a ferritic-martensitic structure with the bright phase to be martensite islands and the darker regions are Ferrite grains

Table 1. Mechanical properties of DP1000 material

	YS(MPa)	UTS(MPa)	Elongation to failure (%)
DP1000	690	1048	16.9

The geometrical parameters were altered as such to ensure the maximum plastic deformation occurs at the free surface of the nugget along the polishing and etching line at the onset of fracture. Therefore, maximum plastic deformation achieved in the cut section was used as the main design criterion for the selected sample geometries under the load. This is because the DIC technique is based on the recorded images of the deforming samples, so it is critically important that maximum plastic deformation and failure occur within the field of view where the strains can be calculated. Nonlinear elastoplastic FE simulations were carried out using the selected testing boundary conditions, See Section 2.2, while the material properties of the weld section were selected from published literature [33-35]. Damage and fracture of the weld were modelled implementing the Gurson-Tvergaard-Needleman (GTN) model according to the reported results of coach peel and tensile shear tests shown in [36,37]. It is important to note that the FE simulation was done to perform a qualitative study for the dimensional analysis of the samples rather than prediction of failure in this study. The final designed geometries and the obtained optimised dimensions are shown in Figure 2 and **Table** 2, accordingly.

2.2 Characterisation of Plastic Deformation in the Weld Nugget

A bending rig was designed to manufacture Micro/Macro coach peel samples, and the tensile-shear samples were cut from the as received sheet material using Wire-EDM. This provided a consistent dimensional accuracy and reduced the effect of residual stresses in the parts since any dimensional and residual stresses could affect the experienced stress state by the samples and consequently the observed failure modes. The resistance spot welds were produced using a Kawasaki ZX165U welding Robot at The Welding Institute (TWI). A set of welding fixtures were designed and used to locate the samples with respect to the welding gun to ensure a consistent and repeatable weld quality was achieved. While the welding force was kept constant for the macro scale samples (TS and CP), three levels of welding current were used to replicate the extreme of the recommended welding parameters for the selected sheet thickness according to the BS EN ISO 18278 standard. These were adjusted to achieve identical weld nugget diameters of 3.8 mm, 4.8 and 5.9 mm for the applied low (L), medium (M) and high (H) current levels. Several samples were made and tested to evaluate variations in the produced welds and the results are reported for representative samples. The applied welding parameters are shown in Table 3.

After welding, the samples were cut along the predefined lines "cut line" using Wire-EDM shown by the dashed lines in Figure 2. The surfaces were mechanically polished to remove the thermally affected layer by the Wire-EDM process and to reach to the final dimensions indicated by the "polishing line" in the figure. The samples dimensions were continuously measured during this stage to ensure the cut and polished section passes through the centreline of the weld and remaining weld nuggets were equal in size at both sides of the sample.

The macro-scale experiments (Macro CP and Macro TS) were conducted combined with the optical 3D stereo DIC system at a quasi-static deformation rate of 1mm/min using a servo-electric tensile testing frame. In order to achieve high quality speckle patterns, that is the significantly important in deformation characterisation using DIC, an air-brush spray with a fine nozzle was used.

The speckle patterns were generated on the polished surfaces of the samples where the weld zones are exposed an example of which is shown in Figure 3. VIC 3D system from Correlation Solutions [38] was used for the DIC image acquisition and analysis of deformation maps following the standard image calibration procedure. Optical images were captured at a frequency of 4Hz, and the strain values were calculated.

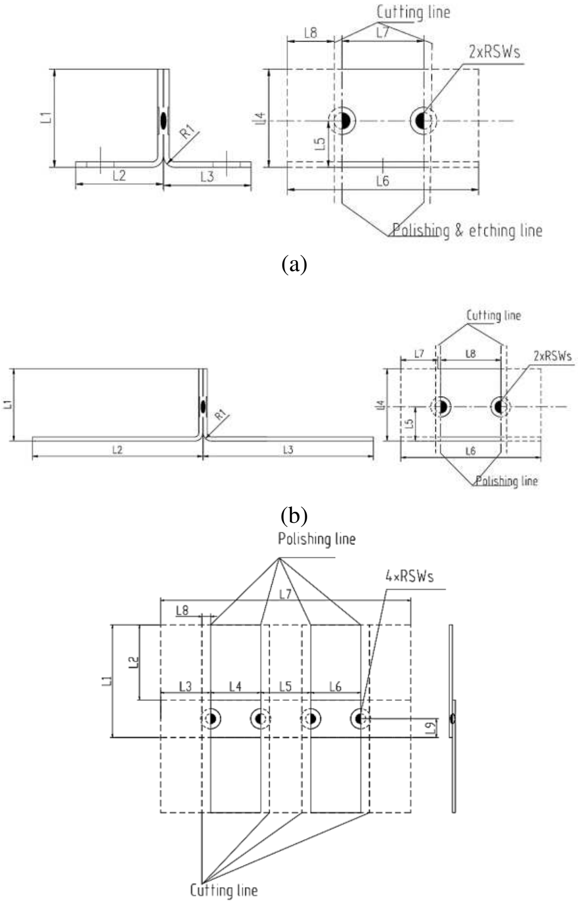

(a)

(b)

(c)

Figure 2. Geometry of samples, (a) micro-CP sample, (b) macro-CP sample and (c) tensile-shear sample (TSS)

Table 2. Dimensions of the designed samples

		Micro-CP(MiCP)	Macro-CP	TS
Dimensional Parameters (mm)	L1	19	23	45
	L2	14.5	40	30
	L3	14.5	40	20
	L4	19	23	20
	L5	10	12	20
	L6	45	50	20
	L7	15	14	100
	L8	14	20	1
	L9	-	-	7.5
	R1	4	4	-

Table 3. Welding parameters of tensile-shear samples and coach-peel samples

Sample	Welding force (kN)	Welding current range (kA)	Welding time (ms)	Holding time(ms)	Nugget size(mm)
TS-L	4	5.5/5.7	320	200	3.8
TS-M	4	6.5/6.7	320	200	4.8
TS-H	4	7.7/7.9	320	200	5.9
CP-L	4	5.5/5.7	320	200	3.8
CP-M	4	6.5/6.7	320	200	4.8
CP-H	4	7.7/7.9	320	200	5.9
MiCP-L	4	5.5/5.7	320	200	3.8
MiCP-M	4	6.5/6.7	320	200	4.8
MiCP-H	4	7.7/7.9	320	200	5.9

The DIC parameters including subset size and the step size were selected to have a minimum of 8 subsets at the region of interests for the thickness of the sheets, as shown in Figure 3a and 3b. The selected parameters ensured there are at least three random features within each subset considering the size of the speckle patterns. To evaluate the effects of the DIC parameters on the obtained results and assess potential errors in strain calculations, a sensitivity analysis was performed and maximum error of less than 5% was recorded in the calibration process. The Lagrangian strain tensor components were then extracted from the measured displacement fields since the materials were experiencing a large plastic deformation.

A Struers DuraScan Vickers micro/macro hardness tester was used, with a 0.5N indentation force, to quantify the hardness profiles variations of the weld sections due to the different welding parameters. Figure 4. shows the cross section of one of the samples with about 30 hardness indents covering the entire weld regions (BM, HAZ and nugget) separated by the allowable minimum distance between the indents according to [39].

To determine the microstructural morphology of the weld sections, the weld nuggets were cut and polished using standard metallography practice using mechanical polishing with Silica followed by etching in a 2% Nital solution [40]. The etched microstructures then examined using optical and scanning electron microscopy (SEM) to determine the effect of welding parameters on the developed microstructural morphologies.

In-situ experiments were conducted on the MiCP samples (Figure 2a) inside the chamber of a Camscan- SEM where the samples were loaded at a rate of 0.2mm/min. The region of interest, i.e. weld nugget, was polished and etched prior to the tests to reveal the microstructural morphologies after the welding, Figure 5. The tests were interrupted at regular intervals of 0.2mm and micrographs of deforming microstructures were continuously recorded at a magnification of 50x after allowing the material to elastically relax. The obtained micrographs, covering the weld nugget and HAZ, were analysed by the DIC technique in which the etched microstructures were used as the random speckle pattern for the image correlation [13]. The measured strain distributions were then mapped on the observed deformation sites.

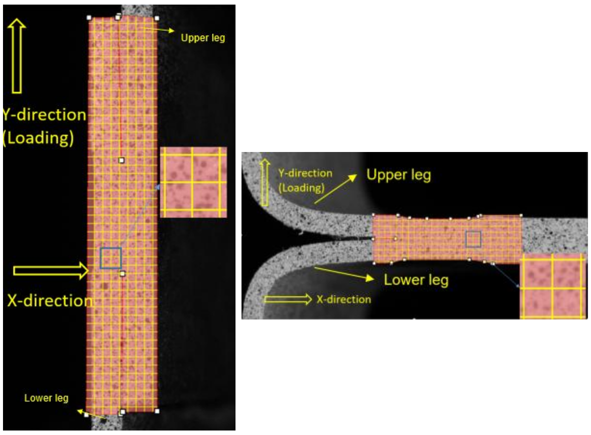

(a) (b)

Figure 3. (a)Tensile shear and (b) Macro Coach peel samples after cutting the weld nuggets in half and preparation for DIC and together with the generated speckle patters showing the size of the selected subsets together with the loading direction.

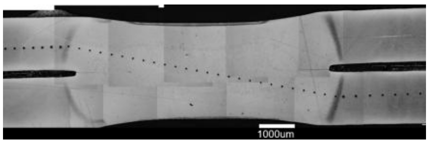

Figure 4. Vickers micro hardness indentation and indents' location on the cross section of a sample.

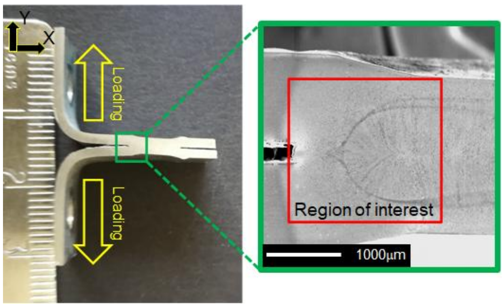

Figure 5. In-situ Micro-CP sample with the highlighted region of interest to study local deformation and failure mechanisms.

3 RESULTS

3.1 Weld Characterization

3.1.1 Metallography and Morphology Analysis of Spot Weld

Figure 6 shows microstructures of different regions the weld zones in DP1000 with applied low, medium and high welding currents. The microstructure of base metal (BM), subcritical heat affected zone (SCHAZ), intercritical heat affected zone (ICHAZ), fine grain heat affected zone (FGHAZ), coarse grain heat affected zone (CGHAZ) and nugget are shown by purple, blue, green, yellow, red and orange colours, respectively. As it was expected and reported in the literature [41], different microstructural morphologies are observed due to the applied heat and cooling rates [42] at the weld section. These start from the base material ferritic-martensitic microstructure at the outer boundary of the weld, Figure 6b, to ICHAZ wherein the martensite volume fraction is slightly increased due to the eutectoid phase transformations followed by rapid cooling(Figures 6g,6l,6q). The materials closer to the nugget, as the centre of heat source, experiences higher temperature for the longer period. Therefore, fine austenite grains are formed with due to the lack of time and thermal energy required the for grain growth. These transfer to fine martensitic structure as it is shown in FGHAZ in Figures 6f, 6k and 6p. The higher temperature at CGHAZ and slightly lower cooling rate allows the grains to grow before rapid quenching generating larger martensite grains (Figures 6e, 6j, 6o). A fully martensitic large lath structure was also observed in the nugget with columnar grains, Figures 6d, 6i and 6n growing from CGHAZ towards the centre of the nugget where grains sizes are slightly smaller compared to the initial solidification phase, Figures 6c, 6h and 6m. It is worth noting that the microstructure between BM and SCHAZ are not significantly different because there is no phase transformation within this zone except the existence of tempered martensite, since the temperature of SCHAZ during welding process is below AC1 [41,43] and the formation of lath martensite might be due to a low carbon content [44].

3.1.2 Microhardness Characterization

Vickers Microhardness profiles of the welded sections are shown in Figure 7 for samples welded at low, medium and high currents using solid square, circle and triangle markers, respectively. While the BM has almost identical hardness, the hardness values instantly drop in SCHAZ in all the cases followed by an prompt increase starting from ICHAZ at the FGHAZ and CGHAZ. This is followed by a small hardness reduction in the nugget. The hardness drop in SCHAZ could be due to the tempering of martensite that reduces its strength. The hardness profiles indicate that by increasing the welding current the overall hardness in all the zones of the weld decreases. Additionally, in the sample welded using the high current, the average hardness value drops more significantly from Fine and Coarse grain zones to the nugget (about 18 HV0.5) compared with the MC (14) and LC (11) samples shown by the blue and red curves, respectively.

3.2 Macroscopic Deformation and Failure Mechanisms

3.2.1 Failure Initiation and Evolution During Loading

The tensile-shear tests were repeated minimum of three times for each case and representative curves are shown in Figure 8a. the solid lines correspond to the TS samples while the dashed lines show the data related to the CP geometries. Figure 8b shows that as the welding current increases the ductility of the weld as well as the fracture forces increase, as expected, for both geometries. The error bars indicate the standard variation of the measured displacement to failure and maximum failure loads between the repeated experiments for each test geometries. Therefore, small error bars in both displacement and failure loads indicate a consistent weld geometry, behaviour and quality for all samples.

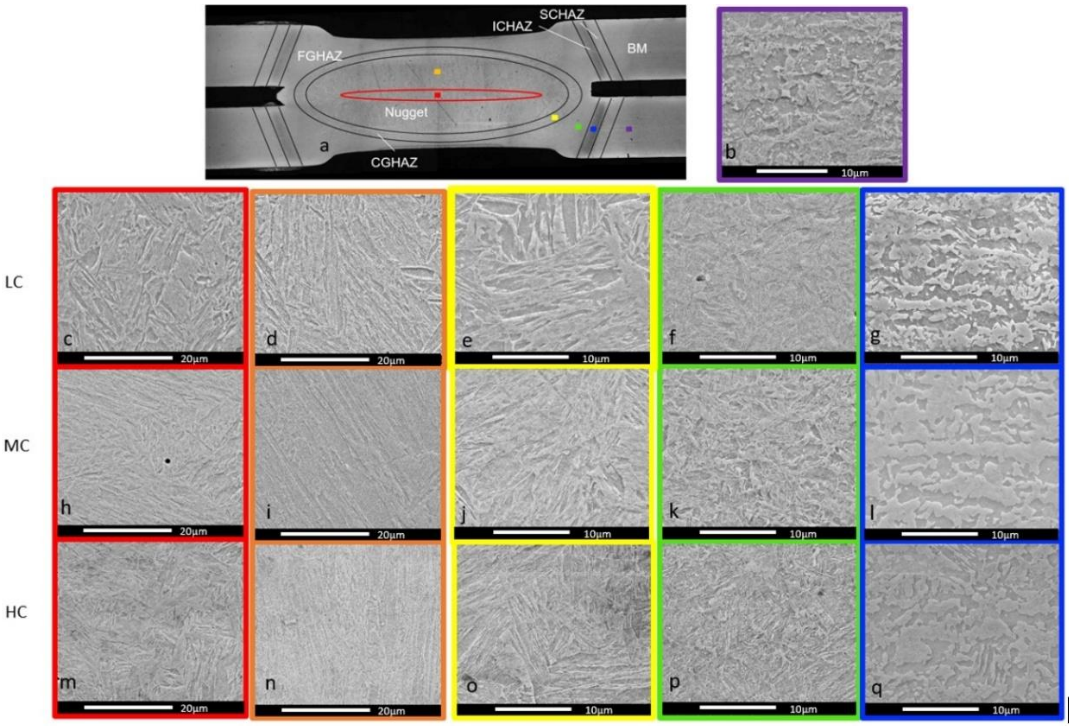

Figure 6. Microstructure of spot welds with applied low (LC), medium (MC) and high welding (HC) currents showing (a) overall section of the weld ; (b) base metal; (c,h, m)and (d, i, n) nugget (Red and Orange); (e, j, o) CGHAZ (Yellow), (f, k, p) FGHAZ(Green) and (g, l, q), ICHAZ(Blue)

It is worth to note that the failure forces in CP samples, the red curves in Figure 8, are an order of magnitude smaller than the forces measured for the TS samples. This could be attributed to the cumulative effect of the bending induced stresses that could be related to the bending moment developed by the applied load in the CP samples leading to smaller required forces as reported in [5]. Additionally, the forces tend to increase linearly in the case of TS samples, Figure 8b, while the CP geometry doesn't show such a behaviour. The longer deformation to failure at higher welding currents results more plastic energy dissipation during the fracture process.

To better investigate the evolving deformation mechanisms during each test, samples with polished sectioned were analysed at different applied displacements up to final fracture as shown in Figures 9 and 10 for TS and CP samples, respectively. Here the localised plastic deformation results in an observable change in the image contrast helping to track the deformation pattern within the weld sections and identify the effect of increasing welding current on the macroscopic failure of the welds.

The deformation and failure in TS-L sample starts with local deformation bands formation at the tip of corona bond shown by the yellow arrow in figure. The deformation is then localised, observed by the change in contrast in the nugget region, shown by the blue arrow in Figure 9c, up to the point that the nugget cannot take further deformation (Figure 9d) and fails by IF mode. There is almost no deformation at upper or lower legs of the sample before, during and after the test. As the welding current increases, TS-M in Figure 9f, local deformation initiation sites move away from the tip of the corona bond, shown by the white arrows, followed by localised deformation at corona bond at later stage. However the interfacial failure is the dominant mode apart from the fact that a relatively large out of plane shear deformation is observed in the sample evidenced by in-plane rotation in the image. Some localized necking was also observed at boundary of HAZ and the base material in TS-M samples as highlighted by the top yellow arrow in Figure 9g. at the same time deformation is transferred to the nugget, shown by the blue arrow. This, however, is not as visible as the case in the TS-L sample. The localised deformation at HAZ promotes additional bending deformation and associated stresses applied to the nugget leading to the mixed mode bending-shear failure mechanism at the nugget. Although, the localised plastic deformation of the material at the HAZ did not change the failure mechanism, the displacement to failure was increased according to Figure 8a.

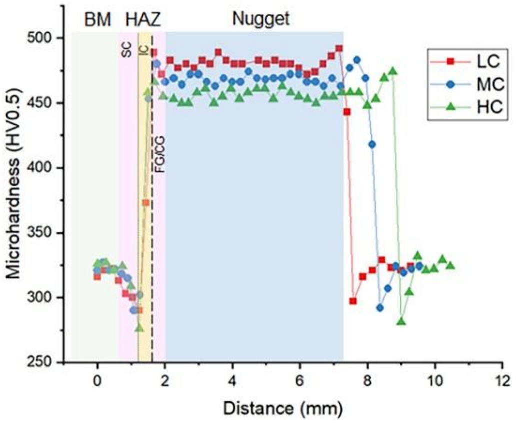

Figure. 7. Comparison of microhardness of spot welds under low welding (square), medium (circle) and high (triangle) welding currents.

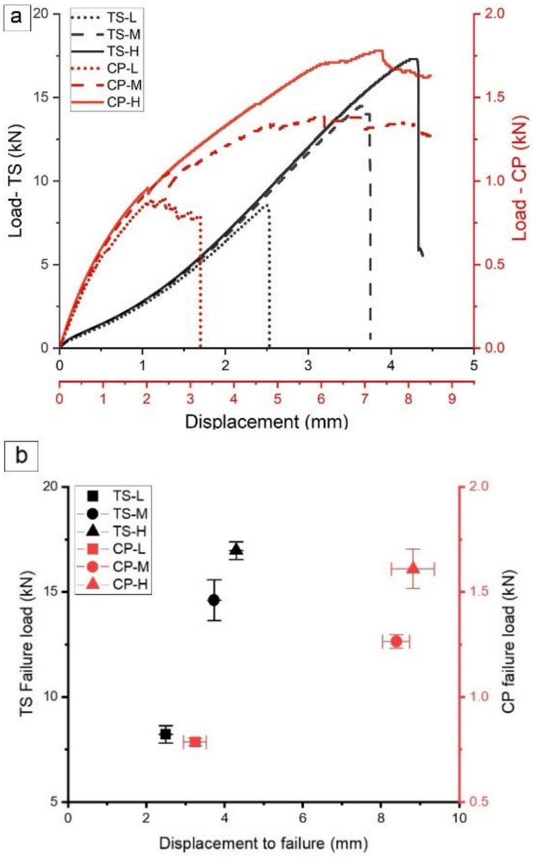

(b)

Figure. 8. Representative measured force-displacement curves during (a) tensile-shear (TS) and coach-peel (CP) tests and (b) maximum force and displacement to failure for the samples welded at low (L), medium (M) and high (H) welding currents. The lines A-F indicate the moment wherein the local deformation maps are further analysed in detail.

The TS-H sample failed via PF mode as shown in Figure 9l. Similar with TS-M sample, deformation localisation is initially observed around the boundaries of HAZ, highlighted with the white arrow in Figure 10j, then transferred to nugget around the corona bond tips shown by the yellow arrows in Figure 10k. However, the plastic deformation located around boundaries of HAZ is much larger than that adjacent to the nugget, Figure 10k. Therefore, it works as plastic hinges during loading and the applied moment resulting in localized necking and ductile fracture of the material at HAZ.

In the case of the coach peel samples, the initial phase of failure involves an opening of the corona bond in all the samples followed by either crack propagation into the nugget, HAZ or the interface of HAZ and nugget depending on the applied welding current. The opening of the corona bond (Figure 10b) introduces a sharp crack at the nugget in CP-L as shown by the yellow arrow. This crack propagates into the nugget, the blue arrow in Figure 10c, resulting in IF mode (Figure 12d). In contrast, two failure initiation sites were observed for CP-M sample at the boundary of the HAZ, the white arrow, and the tip of the corona bond, yellow arrow in Figure 10f. However, due to the bending effect imposed on the samples, failure propagates from the latter into the nugget and deflects to the thickness direction towards the HAZ in the due to the localised necking of the material in this zone, leading to PIF mode, Figure 10h. A pull-out failure was observed in CP-H samples wherein various initiation sites were detected at early stages of deformation, Figure 10j. The localized necking around the nugget deflect the failure line from fusion zone to about 45° with respect to the applied load to the thickness direction.

3.2.2 Local Deformation Characterisation

The recorded images were analysed using a subset and step sizes of 23 pixels and 8 pixels, respectively, and normalised squared difference algorithm [38] was applied for the image correlation process. The out of plane displacement (OPD) maps shown in Figure 11 are representatives of three dimensionality of the deformation in the nugget wherein OPD values in the order of few micrometres were measured for most of the samples. However, the TS-H sample showed the larger OPD with 30µm at the onset of fracture while the maximum in-plane displacement 280µm was measured. Therefore, the out of plane strain component can be negligible compared with the in-plane values and almost a 2D-plane deformation mode can be considered for most of the samples before fracture occurs. In this context, obtained micrographs from in-situ experiments can confidently be used for strain calculations as this level of OPD would have a minimal effect on the SEM micrographs and associated deformation analyses. Additionally, this ensures that the achieved results can be used for the validation of 2D in-plane models of deformation and fracture of spot welds in the future applications.

Figure 12 shows the strain distribution maps in the TS samples with applied low, medium and high welding currents just before the final failure similar to the deformation states shown in Figure 9c, 9g and 9k, respectively. The Lagrangian strain tensor was calculated for X (normal to the loading direction) and Y (parallel to loading) directions as well as shear strain component in the XY orientation. The maximum in-plane principal strain (e_1) was also calculated for each case and given that the out of plane deformation is negligible, it could be considered as corresponding strain at the onset of fracture in the weld section.

The deformation evolution of the Macro-CP samples was analysed at several stages as shown by A-F in the load-displacement curves in Figure 8a. It was found that the e_{yy} (i.e. mode I crack opening) is the main contributor the maximum principal strain (e_1) and dominant deformation mode. Therefore, for the sake of comparison only strain distribution associated with e_{yy} and e_1 are provided for the applied displacements of A- F for CP-L, CP-M and CP-H samples, Figure 13.

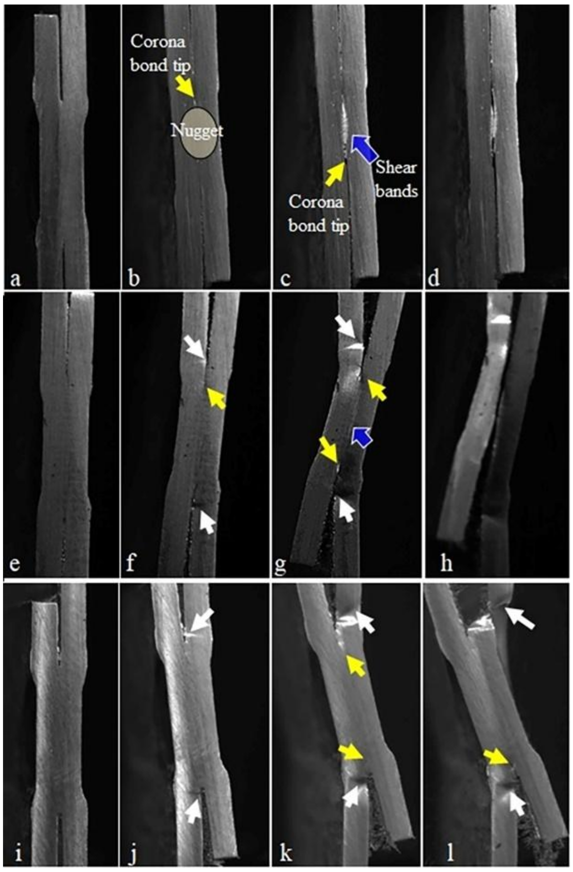

Figure 9. Failure initiation and evolution in TS-L, TS-M and TS-H samples showing different stages of local mechanism with (a), (e) and (i) unloaded samples, (b), (f) and (j) at the onset of plastic yielding, (c) (g) and (k) just before final failure and (d), (h) and (l) final failure. The loading direction is vertical in the images.

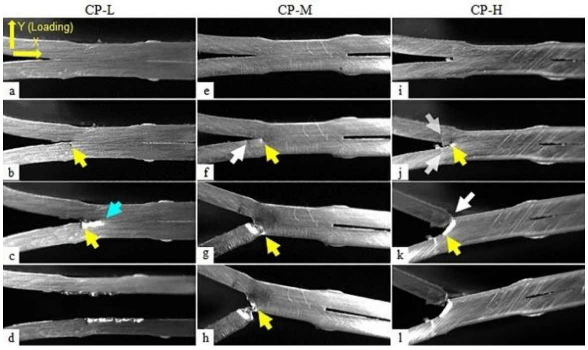

Figure 10. Failure initiation and evolution in CP-L, CP-M and CP-H samples: (a), (e) and (i) image before testing, (b), (f) and (j) around yielding, (c) (g) and (k) just before final failure and (d), (h) and (l) final failure.

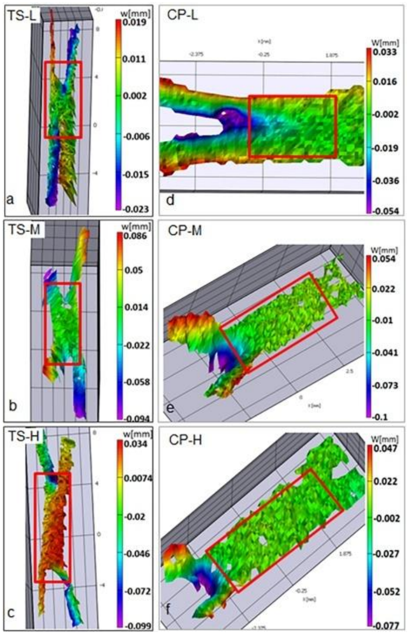

Figure 11. out of plane displacement maps extract for all the samples indicating maximum out of plane displacement of about 30 µm for TS-H sample with other deformation conditions to be considered as 2D-inplane until the onset of fracture

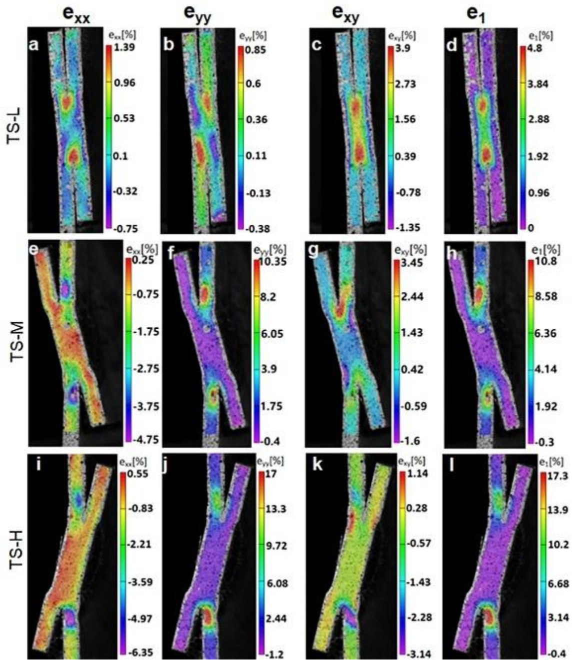

Figure 12. Distribution of strain components for (a-d) TS-L, (e-h) TS-M and (i-l) TS-H samples at the onset of failure showing the strain components normal (a, e, i), aligned to the loading direction (b, f, j), shear (c, g, k) and maximum principal strain (d, h, i).

There is a compressive deformation region in the e_{yy} strain maps ahead of the crack in all the samples (Figure 13a), that for an identical applied displacement, it is smaller in area for CP-L sample while the magnitude of strain is the largest. Additionally, this compressive zone is almost attached to the notch tip in CP-H samples while it was formed further away from the nugget in samples with a lower welding current. The e_{yy} compressive zone moves forward by the applied displacement in the CP-L samples while this propagation is reduced by increasing the welding current and almost it stabilises in the initial location in the CP-H sample. Figure 13b indicates that at an applied displacement of 1.5 mm (point A), e_1 strain value is larger and more localised at the lowest welding current. The measured strain covers larger part of the weld section at the boundary of the nugget, from top to the bottom side of the sheets, in CP-M at point B, while it is heavily localised in CP-L and CP-H at the notch tip and in the interface between HAZ and BM, respectively.

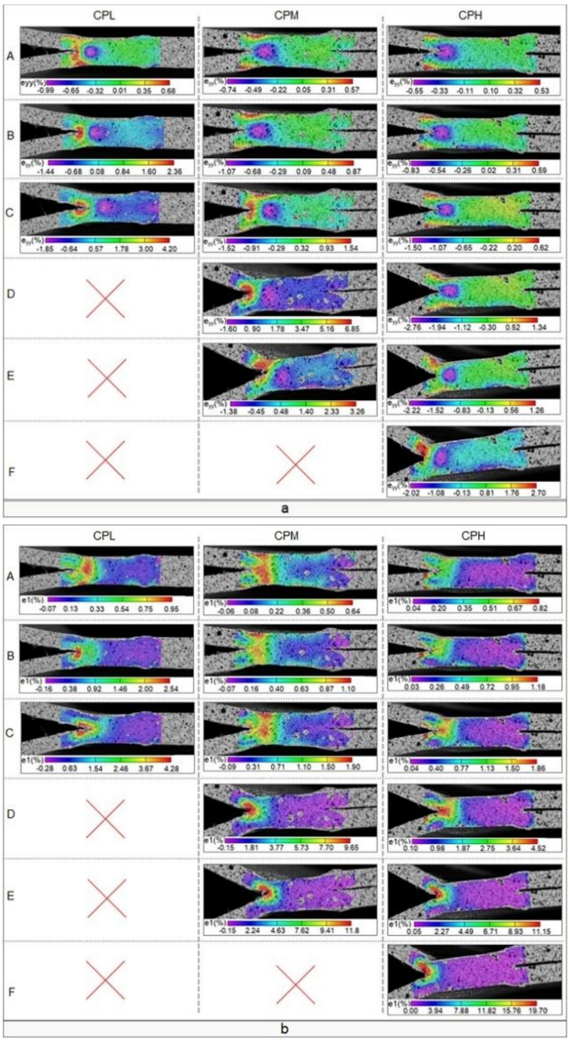

Figure 13. Evolution of local (a) strain distribution along the loading direction (e_{yy}) and (b) maximum principal strain distribution in the weld section of CP-L, CP-M and CP-H samples. The strain maps are extracted for applied displacements of A-F shown in Figure 10a.

The presence of the compressive strain at the vicinity of the notch tip at higher welding current works as a crack retardation mechanism preventing any crack growth into the nugget for CP-M and CP-H samples and forcing the deformation to be localised in other parts of the weld with a higher ductility. However, for the case of the CP-L sample tensile stresses at the notch tip can increase to a critical value facilitating the crack to grow until it is stopped by the developed compressive stresses. It is worth noting that this critical stress at the crack tip changes across different zones in the weld with highest value of about 3% (Figure 13b) recorded in the nugget just before the final failure of CP-L sample at point C. Further applied displacement in CP-M and CP-H samples results in larger plastic deformation in HAZ and BM where e_1 can reach up to about 12% and 20%, respectively. The measured e_{yy} and $e_1$strain values reveal that e_{yy} (the crack opening mode) is the major contributor to the maximum principal strain and subsequently the IF failure of the CP-L sample and IF phase of CP-M sample. This effect is reduced by increase of the welding current. It was found that a tensile deformation along the loading legs and shear deformation in the deformation localised zones are the most contribution factor in e_1 leading to PF in CP-M and CP-H samples.

3.2.3 Fracture Surface Analysis

Micrographs of the fracture surfaces of TS and CP samples are shown in Figures 14 and 15, respectively. Figure 14a shows that the fracture surface in TS-L sample is mostly consist of severely elongated dimples because of shear deformation. However, the dimples geometry changes to more complex fracture mode, including elongated dimples at various directions and pure shear facet, around the circumference of the nugget as highlighted by the yellow region, which could be induced by out-of-plane shear. Elongated dimples are also observed at the fracture surface of TS-M sample, as shown in Figure 14b. However, the central section of the nugget, highlighted by the blue square, shows that dimples are less elongated in the direction of the applied load, in comparison to the observed fracture surface of Figure 14a. Less elongated dimples compared with the central portion of the nugget in various directions are also found to cover a larger part of the surface shown by the highlighted elliptical region away from the tip of corona bond where the failure was observed to initiate from. Since TS-H samples failed at the interface of BM and HAZ, a classical ductile necking and tensile fracture is observed with ductile dimples and shear lips at the edges of the fracture surface as shown in Figure 14c.

A combination of brittle and ductile dimples and brittle facets is observed on the fracture surface of CP-L sample, Figure 15a. The ductile dimples are highly concentrated near the failure initiation site, while brittle fracture features, the red zone, are located where the fracture propagation occurs at the final stages of loading. Although the sample failed through IF mode, the fracture features are fundamentally different than those observed in TS-L sample in Figure 14a wherein the failure is dominated by an early void formation followed by a brittle fracture and no evidence of shear voids across the fracture surface.

The two IF and PF failure modes can be observed at the fracture surface of the CP-M sample shown in Figure 15b. Initially the failure occurs due to Mode I crack opening in the early sections of the fusion zone highlighted by the blue section where a combination of shallow ductile dimples and brittle facets can be seen at the fracture surface. However, in the red section, larger brittle facets are visible as evidence of a catastrophic brittle fracture that could be linked to the larger corresponding martensite grains in the section. The final stage of the fracture, highlighted by the yellow zone, shows shear lips and a typical shear failure like those reported in Figure 14c.

Figure 15c shows the cross section of the failed CP-H samples together with fracture surface morphology in the highlighted zones. Although the sample failed in PF mode, the fracture surface, shown in the red region, indicates that the failure started with a semi-ductile process wherein small ductile dimples are observed among the brittle facets.

These are followed by an almost fully brittle fracture, highlighted in the blue zone, with the failure passing through HAZ/nugget interface and ending with a shear deformation, in the yellow section, towards the end of the test. A relatively small proportion of brittle facets on the fracture surface compared with CP-M and CP-L samples indicates that although there are some parts of the nugget failing by brittle fracture, the ductile void initiation and coalescence is the dominant mechanism in CP-H sample.

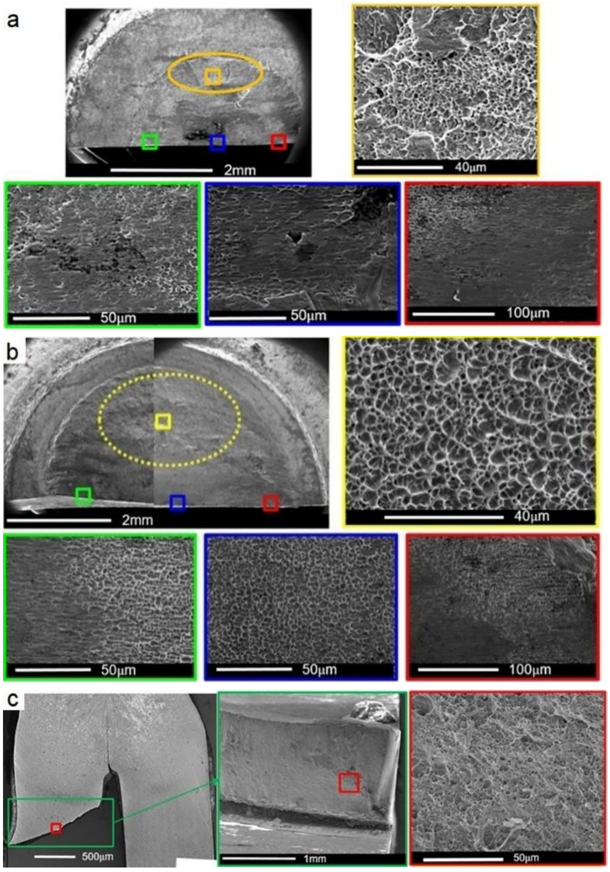

Figure 14. Fracture surfaces showing domination of (a) ductile and shear failure in TS-L, (b) ductile failure in TS-M and (c) local necking and ductile failure in TS-H samples.

3.3 Microscopic Failure Characterisation of the Welds

Figure 16 shows representative measured load-displacement curves for the in-situ experiments wherein MiCP samples were tested. The samples were not loaded to final fracture due to limited available cross head displacement, but failure initiation and propagation mechanisms were captured in the recorded micrographs. The sample welded using the higher current, MiCP-H, the black curve in Figure 16, showed the highest resistance against the applied load while MiCP-L, the red curve, experience a near complete fracture. The stage was stopped at every 200 micron and samples let to elastically relax for about 3 minutes before micrographs of the deforming microstructures were captured. The load drops in the curves show the imaging intervals when the stage was stopped and consequently the measured loads drop due to the elastic relaxation of the system. Micrographs of the samples corresponding to the selected points (shown by arrows in Figure 16) during loading are shown in Figures 17 and 18. The loading direction is vertical in the micrographs as indicated by the arrows.

In the case of MiCP-L, the sample welded with the lowest welding current, the failure initiates by opening of the corona bond at the early stages of the loading, white arrow in Figure 17b. This is followed by plastic deformation localisation when the generated crack reaches the boundaries of the nugget and CGHAZ, Figure 17c. Deformation bands appear in the nugget as a result of the deformation localisation up to a point that cracks form at the tip of corona bond as shown in Figure 17d. One crack is formed to follow the microstructure in the CGHAZ, the red arrow, round the nugget while the other, indicated by the black arrow, is directed towards the centre of nugget where the material last solidified in the Figure and the enlarged subfigure.

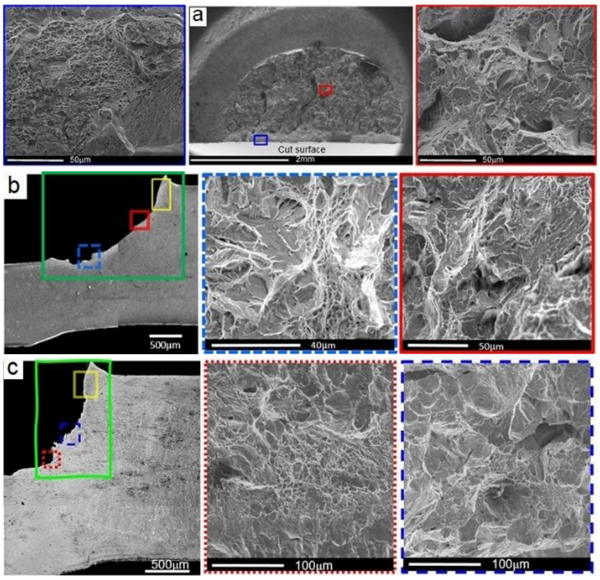

Figure 15. Fracture surface of CP samples showing domination of (a) quasi-cleavage failure in CP-L, (b) quasi-cleavage and shear failure in CP-M and (c) ductile and shear failure in CP-H samples.

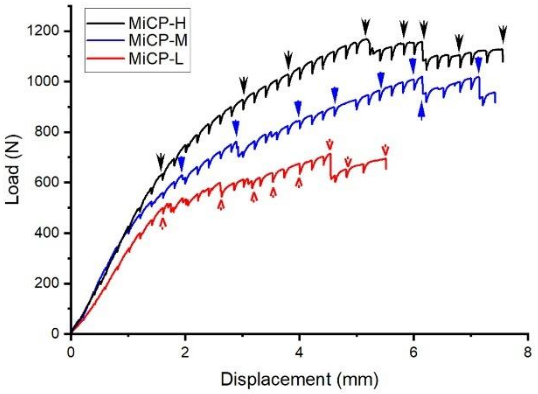

Figure 16. Force-displacement curve of coach-peel samples with low (MiCP-L), medium (MiCP-M) and high (MiCP-H) welding currents.

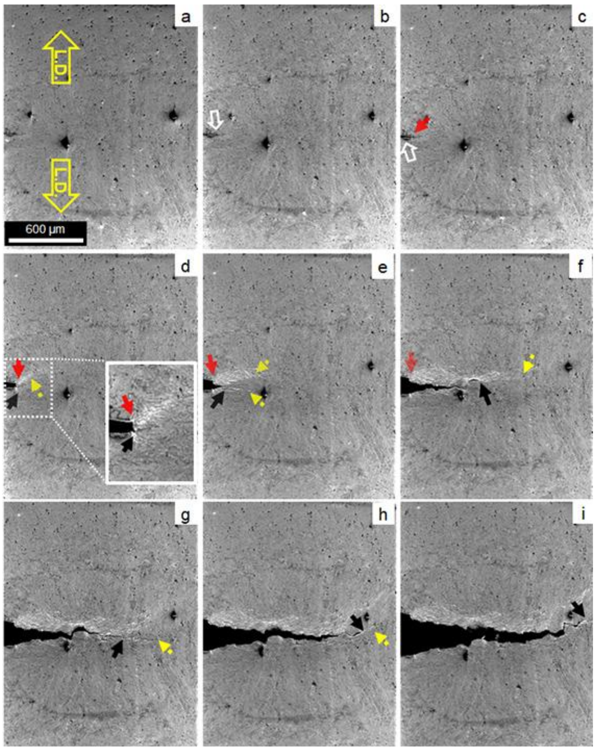

Figure 17. Crack propagation of MiCP-L sample at various stages of loading shown in Figure 18. The loading direction is vertical in the micrographs. The yellow arrows show localized deformation bands formation, the red and black arrows indicate the cracks form in the microstructure with the failure propagations shown by the latter.

The dominant crack, shown by the black arrow, follows the deformation bands, shown by the yellow arrows, in such a way that the crack propagates normal to the grains at the middle of the nugget with some minor deflections as shown in Figures 17f to 17i. The deformation bands indicate that the observed IF failure in the tested samples is associated with a level of plastic deformation in the martensite grains within the nugget.

The failure process in the MiCP-M sample, Figure 18I, starts with opening of the corona bond, as was the case for MiCP-L sample, creating a sharp crack at the interface of HAZ and the nugget, Figure 18Ib. The large stress concentration develops plastic deformation in the form of shear bands, visible by the change of contrast in the micrograph in Figure 18Ic which results in the crack bifurcation in the nugget. The two cracks, shown by the red and black arrows, in Figure 18Id, further propagate into the nugget. The dominant crack is then formed (Figure 18Ie) and propagates along the martensite grains before it is deflected at about 45° towards the outer surface of the nugget as shown by the black arrow in Figure 18If,. This dominant crack is then opened throughout the test, Figure 18Ih, and it is expected to pass through the dashed red line in Figure 18Ii .

Micrographs of Figure 18II show failure initiation and propagation mechanisms for PF model observed in MiCP-H sample. The loading direction is shown by the arrows in Figure 18IIa and after the early stages of deformation the crack initiated by the corona bond is arrested at the boundary with the nugget, the red arrow in Figures 18IIc, d. Although some deformation localisation is observed in the nugget, shown by the yellow arrow in Figure 18IId, the crack is deflected into the HAZ passing from CGHAZ into FGHAZ (black arrow in Figure 18IIe,f). The deformation bands are developed within the HAZ and define the crack path. However the crack propagation was confined by smaller grains in the FGHAZ and was deflected into the CGHAZ at the later stages of the deformation (Figure 18IIg). Although the final fracture was not achieved, failure is expected through the highlighted dashed line in Figure 18IIh by a shearing process to complete the final phase of the pull-out failure mode.

Figure 19 shows the strain maps corresponding to Figures 17 and 18 to better understand the evolution of deformation at identified damage mechanisms. The deformation patterns measured in the in-situ experiments generally follows those obtained in the Macro-CP samples. Therefore, only the e_1 strain component is reported for this section. The undeformed micrographs are not shown in Figure 19. The strain maps show a largely localised deformation in the central part of the nugget for MiCP-L sample, while for the other two samples a significantly bigger section of the nugget experiences a larger plastic deformation. This partially explains the measured higher forces during the experiment before the initiation of damage and fracture.

At the onset of crack initiation in sample MiCP-L (Figure 19 MiCP-L(c)) the white arrow indicates that the crack is entering the nugget at the interface with the corona bond at a measured local strain of about 1.9%. The previous step of loading in this samples indicates a very small compressive strain that could be due to initial bending moment applied by the loading and the fact that the observed area does not fully cover the borders of the deforming region.

As the crack propagates through the nugget, Figure 19 MiCP-L(d) and MiCP-L(f), shear bands appear on the microstructure well ahead of the crack revealing damage initiation and localised necking in the material. The strain values at the onset of shear bands formation were found to be consistently around 3% throughout the loading process. However localised deformation at the crack tip was not measured due to the missed correlation in the image processing algorithm.

On the other hand, for the case of MiCP-M sample at the onset of damage initiation when the crack enters the nugget (the darker region in the nugget indicated by the red arrow in Figure 19 MiCP-M(b)) local maximum principal strain value of about 2% was measured.

The local deformation in the nugget where shear bands become visible shown by the yellow arrows in Figure 19 MiCP-M(c) and MiCP-M(e) increases to about 6%. The plastic deformation at the surface increases while the deformation bands develop further until cracks appear and propagate, therefore larger strains were measured at the vicinity of the crack. As the crack is deflected towards the top surface in the nugget (Figure 19 MiCP-M(f) and MiCP-M(g)) the localised strain gradually increases to about 8%. This could be an indication of modified mechanical properties across the microstructure of the weld nugget considering that the stress state is not changing significantly. Local strain at the start of deformation and damage for MiCP-H sample is almost similar to the previous samples (Figure19 MiCP-H(b)), however the shear banding and plastic instability was observed in both the nugget (the yellow arrow) and HAZ (the blue arrow) as shown in Figure 19 MiCP-H(e). While the localised strain of about 8% was observed in the localised necking of the nugget microstructure, the blue arrows in the MiCP-H maps show that FGHAZ deformed slightly less (about 9%) compared to the CGHAZ where maximum principal strain of about 12% was measured (Figure 19 MiCP-H(g)).

4 DISCUSSIONS

4.1 Metallography and morphology analysis of the welds

The characterisation of microstructural morphology of the samples indicated that the microstructure of different weld zones was greatly affected by the applied welding current. The higher welding currents produced larger nuggets due to the increased thermal energy and consequently generated bigger fusion zone under the electrodes. The heat input from the electrodes and the subsequent rapid cooling promotes a martensitic transformation and grain growth [32]. Due to the faster cooling rate of the nugget close to the water-cooled electrodes, longer columnar grains form at upper and lower side of the nugget while the columnar grains are shorter where the weld zone is cooled through air and base metal [8]. The martensite grains contain lath type martensite that are shorter and smaller in size in the central region of the nugget where solidification of the melt pool terminates, Figure 6.

The variation of the local hardness can directly be linked to heat treatment of the base microstructure during the applied heating and cooling cycle of the weld as reported in [42,45].

The SCHAZ is subjected to lower temperature, therefore the microstructural morphology is not significantly changed, however martensite hardness drops because of the tempering effect on the local hardness of the material. The increase of local hardness in ICHAZ could be linked to a higher martensite volume fraction as the temperature reaches above AC1 [41], therefore more ferrite is transformed to martensite by the rapid cooling .[46]

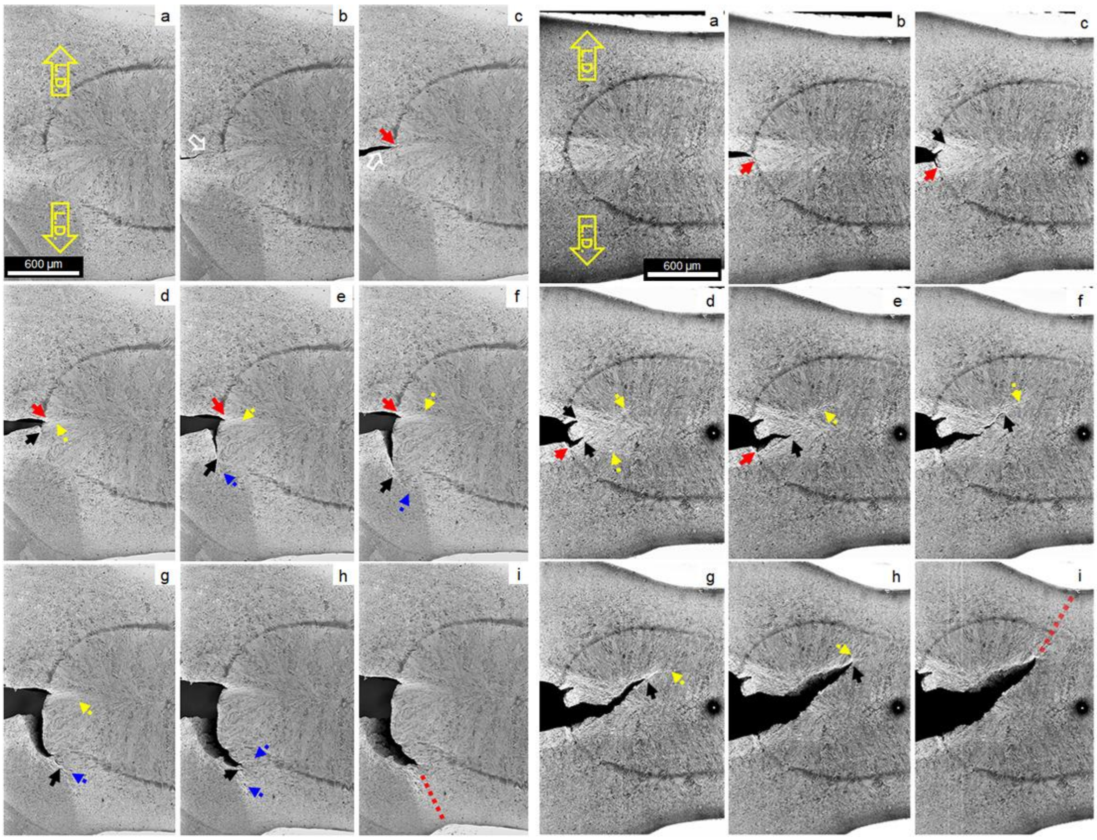

(I) (II)

Figure 18. Evolution of failure in (I) MiCP-M and (b) MiCP-H samples showing the mechanism of partial IF and pull-out failure modes, respectively. The loading direction, L.D, is vertical in the micrographs and the yellow and blue arrows show the deformation bands while the black arrow highlights the dominant crack.

The recrystalised grains in FGHAZ are much smaller than the base metal, so a sharp rise in the local hardness value is expected. Increasing volume fraction of martensite in the microstructure from ICHAZ to the nugget results in an increased hardness, however larger grain size of CGHAZ the nugget induces slight reduction of the measured hardness value.

The increasing welding current from 5.5kA to 7.7kA results in increased thermal energy input from 23J to 46J, respectively, in the material that can prolong the heating cycle. This increased heating with a reduced cooling rate increases the ductility of the weld section [47]. Since the local hardness is directly linked to the yield strength of steel alloys [48], therefore, the lower hardness supports the formation of a deformable nugget in the samples welded at higher currents as also reported in[49] .

4.2 Deformation Mechanisms in Tensile-Shear Loading

The evolution of local strain at the centre of the nugget (location 1) and around the corona bond tip (location 2) are shown in Figure 20 for the TS samples. The shear strain evolution is almost identical to the maximum principal strain in TS-L sample, at location 1 and 2 indicating, Figure 20d. According to the strain evolution curves, the material is gradually deformed in both locations, albeit with a different rate, resulting in a relatively uniform stress and strain distribution within the weld section. The high stress values at the tip of corona bonds could have initiated the failure process in the shear mode considering the small size of the nugget [6]. Additionally, given the higher hardness of the nugget and the applied deformation, the required surface energy to develop a crack into the nugget can be easily achieved. Smaller grains are reported to form at the final stages of the solidification process [2] where deformation localisation is observed for the samples welded using the lower currents (Figure 19). Therefore, lower mechanical strength is expected for this section making it the failure initiation site for the failure under IF mode.

At the medium welding currents (TS-M sample), e_{yy} and e_{xy} strain evolutions are similar and much larger than e_{xx} strain at corona bond tip while there is almost no deformation in the material within centre of nugget, shown in Figure 20e.

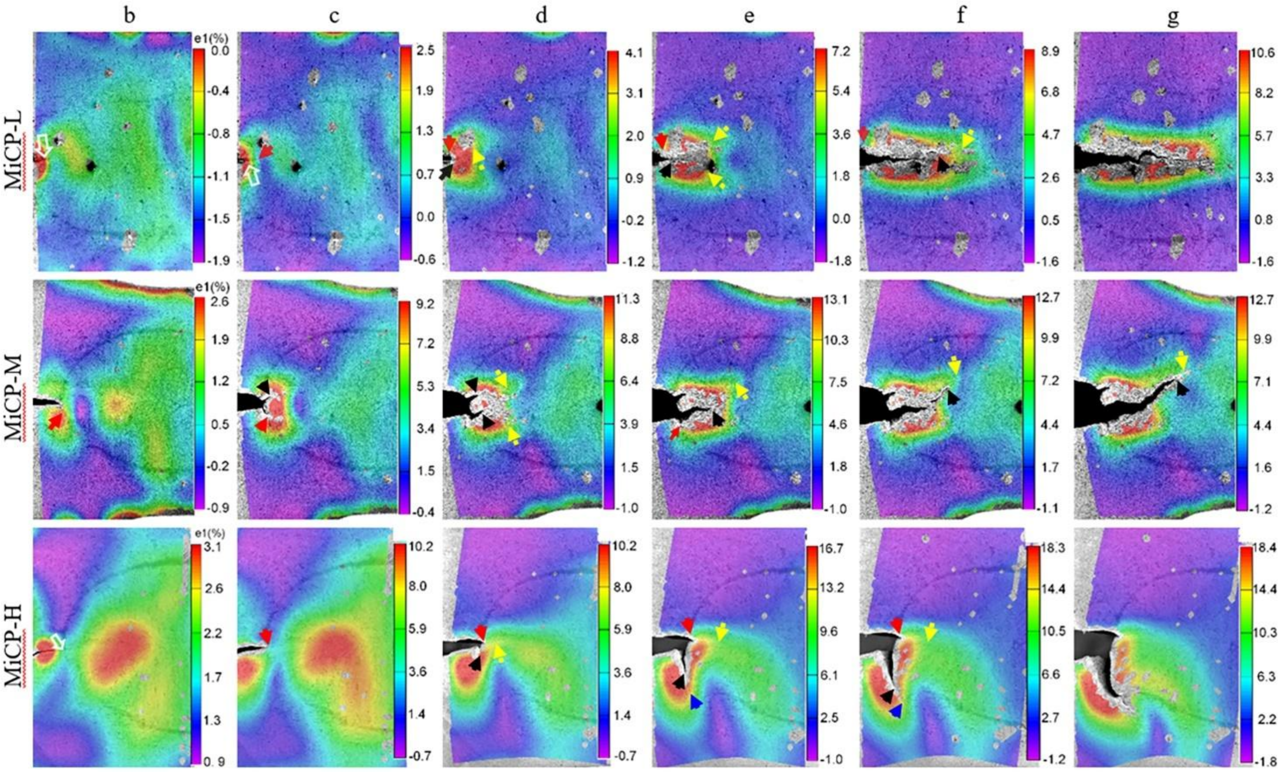

Figure 19. Distribution of maximum principal strain component for MiCP-L, MiCP-M and MiCP-H samples at loading intervals identical to those shown in Figures 17 and 18. The arrows highlight the location of identified damage/fracture mechanisms in the microstructure as demonstrated in the previous figures.

As the welding current increases a softer HAZ is formed which enables a larger plastic deformation to occur at the stress concentration points and crack tip. This helps to dissipate the internal energy in the whole nugget and consequently reducing the stress transfer from the HAZ to the nugget. Additionally, the larger diameter of the nugget in TS-M samples the overall stress will also be reduced retarding fracture process .

In TS-H sample (Figure 20f), e_{yy} strain evolution is almost consistent with the maximum principal strain curve at the corona bond tip and there is almost no sign of deformation due to the shear mode indicating tensile deformation developed in Y direction dominates the failure. According to the fracture surface, the fracture mode is a combination of mode I and mode II. In contrast to the other samples, there is a compressive e_{xx} strain evolution at the corona bond tip in TS-H sample that could be linked to the local necking of the material at the selected point. The maximum principal strain increases from around 5% to around 8% at the corona bond tip just before crack initiation as welding current, and subsequently the fusion zone size, increases indicating that material within the nugget can withstand larger plastic deformation and consequently require more applied energy (higher failure load and longer elongation) for fracture propagation through the nugget, Figure 20g .

The e_1 values in the central nugget (location 2 in Figure 20) at the onset of failure reduces from around 2% for TS-L to close to zero for TS-M and TS-H samples. Both the HAZ and nugget become softer by increasing the welding current, Figure 7, however the maximum principal strain values in locations 1 and 2 indicates that the HAZ softening effect would be the dominant factor affecting the failure mechanism. Additionally, a larger and softer nugget is achieved by a higher welding current resulting in a higher required fracture energy while the deformation localisation in the HAZ leads to a lower stress evolution in the nugget. This makes the nuggets formed at a higher welding current to be more fracture resilient.

In-plane shear dimples have also been observed at the central part of the nugget section for full welds DP980[3,8], and out of plane shear at circumference of nugget fracture surface was reported by researchers which is similar with observation in the fracture surface of TS-L. However, quasi-cleavage fracture was reported to be the dominant fracture mode of IF failure in B1500 steel, which differs from the observed fracture mechanism in TS-L sample. This could be due to the material in the nugget of B1500 steel is much harder that makes the nugget harder to be plastically deformed.

Although, TS-M sample shows a similar fracture mechanism with TS-L sample, larger bending and stretch in HAZ/nugget due to softening of the weld section, Figure 20, could apply more complex stress state to the nugget leading to larger portion of out-of-plane shear fracture. In TS-H sample, necking occurred in HAZ/ BM where has lower hardness due to lower cooling rate that results in lower dislocation density is the main reason to induce Pull-out failure [50,51]. Additionally, out of plane shear during IF mode was also found to be dominant in materials with higher strength as reported in [5].

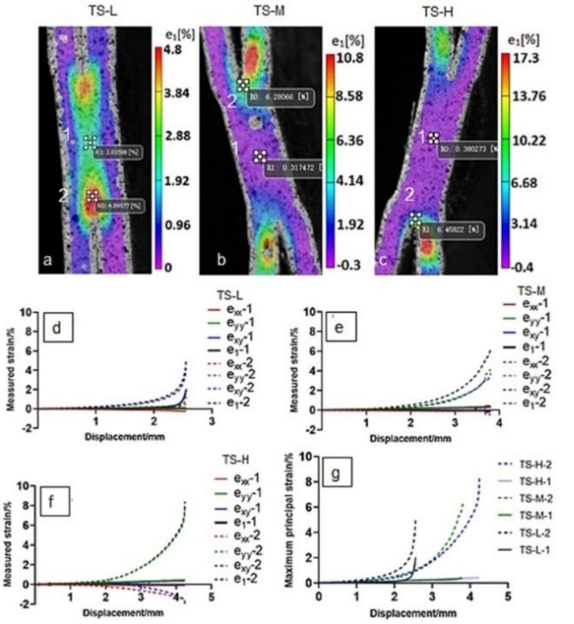

Figure 20. Measured strain evolution curves between start point of deformation and start of failure of (a) and (d) TS-L, (b) and (e) TS-M, (C) and (f) TS-H samples and (g) comparison of maximum principal strain at centre of nugget and around corona bond tip within the nugget under low, medium and high welding currents.

4.3 Deformation Analysis Under Coach-Peel Loading Condition

It is already reported that HAZ softening improve ductility of the spot welds leading to a higher energy absorption [52]. Fracture toughness of the weld section is reported as the most effective parameter in assessing mechanical properties of the welds [53,54]. Chabok et al. [41] developed a methodology to determine fracture toughness of individual sections in a spot weld of DP1000 steel. However, there is limited information on the deformation mechanics and associated distribution in the weld and its effect on failure process. It is shown, in Figure 13, that the presence of a compressive stress filed in front of the crack in the coach peel samples could affect the crack propagation and failure mechanisms. This effect is enhanced by the formation of low angle grain boundaries in the CGHAZ and smaller martensite grains in the FGHAZ [43].

Figure 21 shows the evolution of strain at the corona bond tip for the CP samples by the applied displacement to the point that a critical crack is formed in the samples (Figure 21a to 21c). It is already reports that crack opening mode (mode I) is the main loading condition in the CP samples [4,5]. Although e_{yy} strain component starts with a compressive trend in all samples, it sharply changes to the tensile state for CP-L and CP-M samples after about 1mm and 2mm of applied displacement, respectively. The compressive strain is the largest for the higher welding currents indicting a negative stress intensity factor (K_I), preventing the crack to propagate in mode I fracture [55]. Additionally, e_{yy} strain status does not become positive in the CP-H sample up to the point that a failure is observed, so no crack propagation normal to the loading direction should have been expected in these conditions promoting a pull-out failure outside the HAZ.

At the higher welding currents the contribution of e_{xx} strain component, i.e. stretching of the loading legs, significantly increases (Figure 21e and f) dominating the deformation condition in CP-H sample (Figure 21f). The fact that e_{yy} and e_{xx} jointly affect the development of maximum principal strain in CP-M sample shows that the failure is expected to be due to a mixed tensile- shear (mode II) crack propagation. The strain evolution of CP-H sample shown in Figure 21f, which is the first part of failure (highlighted in the white square labelled as " f "), indicates that material within the corona bond tip goes under tension in X direction while strain e_{yy} is in compression mode, thus forming a localised necking zone.

For the second part of PF mode shown in Figure 21g, the shear strain curve is almost consistent with maximum principal strain curve indicating that shear deformation controls the second part of PF mode until normal strain in X direction become dominant leading to the formation of tensile failure at the BM .

According to the deformation evolution analysis above, increasing the welding current results in softening of the weld section as shown by the hardness profiles. This softening effect is found to be more effective in reducing the mechanical strength of the HAZ compared with the fusion zone as the tempering effect could have more influence on reducing dislocation density in FGHAZ reported to have higher yield and lower strain hardening [41]. This was better observed in the Mi-CP samples (Figures 17 and 18) where the crack is pushed further into the HAZ by increasing the current due to the increased plasticity and reduced stiffness. Therefore, a larger plasticity observed at tip of corona bond and within the FGHAZ by increasing the welding current together with the formation of the compressive deformation zone in the nugget affects the failure mode transition from IF to PF.

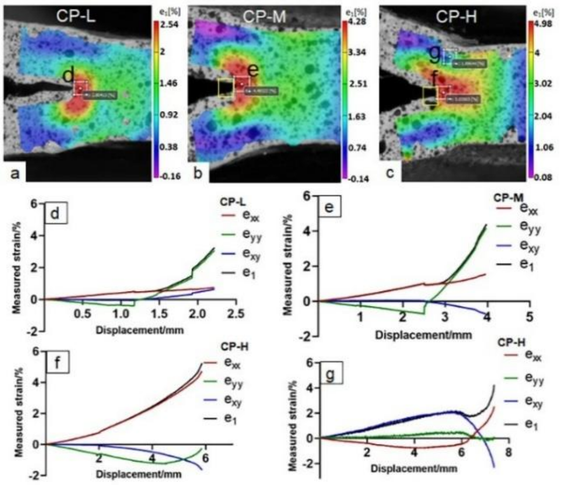

Figure 21. Maximum principal strain distribution, (a) CP-L, (b) CP-M and (c)CP-H, indicating the extracted positions of strain evolution curves between start point of deformation and crack initiation of (d) CP-L, (e) CP-M and (g) CP-H samples while (h) strain evolution curves between start point of loading and final failure of second phase of PF mode in CP-H samples.

5 CONCLUSIONS

The experimental results prove that the designed sample geometries are effective to investigate the influence of deformation evolution to failure mechanism of spot weld in AHSS, not only in macro scale but also in micro scale. Specific conclusions on the deformation and failure mechanisms of the studied spot welds are as follows:

1. HAZ softening induced by increasing welding current according to hardness analysis of welding section can lead to the transition of failure modes from IF mode to PF mode of TS samples. Shear stress within the nugget causes IF mode and stress along Y direction as well as shear stress in HAZ and BM dominates PF mode.
2. Larger bending due to HAZ softening in CP samples leads to compression normal to interface of nugget for longer elongation and larger plastic deformation in HAZ causing transition of IF mode to PF mode. Stress normal to the interface of nugget is the driving force IF mode while bending stress and shear stress in HAZ is the driving force of PF mode.
3. The smaller martensitic laths within centre of the nugget might resist the crack from passing through the nugget in CP samples leading to crack path deflection.
4. A better ductility of weld section could be obtained by higher welding current.

6. ACKNOWLEDGEMENTS

The authors would like to thank the financial and technical support provided by Tata Steel Europe to conduct this research. Technical contribution of TWI for manufacture of samples is greatly acknowledged.

7. REFERENCES

1. Dancette S, Fabrègue D, Massardier V, et al. Experimental and modeling investigation of the failure resistance of advanced high strength steels spot welds. Engineering Fracture Mechanics. 2011;78(10):2259-2272 https://doi.org/10.1016/j.engfracmech.2011.04.013

2. Bouzekri M, Dancette S, Dupuy T, et al. An investigation of failure types in high-strength steel resistance spot welds. Welding in the World. 2010;54(3-4):3-14 https://doi.org/10.1007/BF03263485

3. Dancette S, Massardier-Jourdan V, Merlin J, et al., editors. Investigations on the mechanical behavior of advanced high strength steels resistance spot welds in cross tension and tensile shear. Advanced Materials Research; 2010; 89-91: 130-135 https://doi.org/10.4028/www.scientific.net/AMR.89-91.130

4. Pouranvari M, Marashi SPH, Jaber HL. DP780 dual-phase-steel spot welds: critical fusion-zone size ensuring the pull-out failure mode. Mat Technol. 2015;49:579-585 https://doi.org/10.17222/mit.2014.184

5. Pouranvari M, Marashi S. Failure of resistance spot welds: tensile shear versus coach peel loading conditions. Ironmaking & Steelmaking. 2012;39(2):104-111 https://doi.org/10.1179/1743281211Y.0000000066

6. Pouranvari M, Marashi S. Similar and dissimilar RSW of low carbon and austenitic stainless steels: effect of weld microstructure and hardness profile on failure mode. Materials Science and Technology. 2009;25(12):1411-1416 https://doi.org/10.1179/026708309X12459430509292

7. Pouranvari M, Ranjbarnoodeh E. Dependence of the fracture mode on the welding variables in the resistance spot welding of ferrite-martensite DP980 advanced high-strength steel. Materials and Tehnology. 2012;46(6):665-671

8. Dancette S, Fabregue D, Massardier V, et al. Investigation of the tensile shear fracture of advanced high strength steel spot welds. Engineering Failure Analysis. 2012;25:112-122 https://doi.org/10.1016/j.engfailanal.2012.04.009

9. Radakovic D, Tumuluru M. An evaluation of the cross-tension test of resistance spot welds in high-strength dual-phase steels. Welding journal. 2012;91(1):8-15

10. Yao Z, Omiya M, Ma N, et al. Local mechanical characterization and fracture prediction modeling for resistance spot-welded joints of advanced high-strength steel. Materials Today Communications. 2023;36:106787 https://doi.org/10.1016/j.mtcomm.2023.106787

11. Huin T, Dancette S, Fabrègue D, et al. Investigation of the failure of advanced high strength steels heterogeneous spot welds. Metals. 2016;6(5):111 https://doi.org/10.3390/met6050111

12. Alharbi K, Ghadbeigi H, Efthymiadis P, et al. Damage in dual phase steel DP1000 investigated using digital image correlation and microstructure simulation. Modelling and Simulation in Materials Science and Engineering. 2015;23(8):085005 https://doi.org/10.1088/0965-0393/23/8/085005

13. Ghadbeigi H, Pinna C, Celotto S & Yates JR. Local plastic strain evolution in a high strength dual-phase steel. Materials Science and Engineering: A. 2010, 527 (18-19). pp. 5026-5032, https://doi.org/10.1016/j.msea.2010.04.052

14. Vautrin A, Lee JR, Molimard J, et al., editors. Full-field optical techniques: Applications to strain measurement and mechanical identification. 10th European Conference on Composite Materials (ECCM10); 2002

15. McKelvie J. Moire strain analysis: an introduction, review and critique, including related techniques and future potential. Journal of Strain Analysis for Engineering Design. 1998, 33(2):137-151 https://doi.org/10.1243/0309324981512878

16. Díaz-Garrido EL-AaFA. Full-Field Indentation Damage Measurement Using Digital Image Correlation. Materials 2017, 10(7), 774; https://doi.org/10.3390/ma10070774

17. Tong Wu MC, Alain Combescure. Strain Localisation and Damage Measurement by Full 3D Digital Image Correlation: Application to 15-5PH Stainless Steel. Strain, 2011, 47 (1), pp.49-61.

https://doi.org/10.1111/j.1475-1305.2008.00600.x

18. Ghadbeigi H, Pinna C, Celotto S. Failure mechanisms in DP600 steel: initiation, evolution and fracture. Materials Science and Engineering: A. 2013;588:420-431, https://doi.org/10.1016/j.msea.2013.09.048

19. Siebert T, Becker T, Spiltthof K, et al., editors. Error estimations in digital image correlation technique. Applied Mechanics and Materials; 2007; 7-8: 265-270 https://doi.org/10.4028/www.scientific.net/AMM.7-8.265

20. Vassoler J, Fancello E. Error analysis of the digital image correlation method. Mecánica Computacional. .2010;29(61):6149-6161

21. Pan B, Xie H, Wang Z, et al. Study on subset size selection in digital image correlation for speckle patterns. Optics express. 2008;16(10):7037-7048,

https://doi.org/10.1364/OE.16.007037

22. Midawi A, Shojaee M, Mohamadizadeh A, et al. A novel technique to measure the local mechanical properties of third generation advanced high strength steel resistance spot welds. Forces in Mechanics. 2022;9:100150,

https://doi.org/10.1016/j.finmec.2022.100150

23. Shojaee M, Betiku O, Tolton C, et al. Investigating the Mechanical Properties and Failure Behavior of Groups of Resistance Spot Welds under Tensile-Bending Loading Conditions. Journal of Materials Engineering and Performance. 2025:1-20,

https://doi.org/10.1007/s11665-025-10798-2

24. Shojaee M, Tolton C, Midawi A, et al. An experimental methodology to characterize load-based fracture models of third generation advanced high strength steel resistance spot welds. The International Journal of Advanced Manufacturing Technology. 2024;132(1):943-965, https://doi.org/10.1007/s00170-024-13438-6

25. Mohamadizadeh A, Biro E, Worswick M. Shear band formation at the fusion boundary and failure behaviour of resistance spot welds in ultra-high-strength hot-stamped steel. Science and Technology of Welding and Joining. 2020;25(7):556-563, https://doi.org/10.1080/13621718.2020.1773057

26. Mohamadizadeh A, Biro E, Worswick M. Failure characterization and meso-scale damage modeling of spot welds in hot-stamped automotive steels using a hardness-mapping approach. Engineering Fracture Mechanics. 2022;268:108506,

https://doi.org/10.1016/j.engfracmech.2022.108506

27. Mohamadizadeh A, Biro E, Worswick M. Novel double-half spot weld testing technique for damage progress and failure analysis using digital image correlation techniques. Experimental Mechanics. 2021;61(9):1405-1418, https://doi.org/10.1007/s11340-021-00743-4

28. Yu F. Investigation of failure mechanisms of resistance spot welds in automotive steels using various techniques: .University of Sheffield; 2020

29. Committee A. Standard Test Methods for Tension Tesing of Metallic Materials (E8/E8M − 13a). Retrieved from .www.astm.org 2013

30. Chen N, Wang H-P, Carlson BE, et al. Fracture mechanisms of Al/steel resistance spot welds in coach peel and cross tension testing. Journal of Materials Processing Technology. 2018;252:348-361, https://doi.org/10.1016/j.jmatprotec.2017.09.035

31. Daneshpour S, Kokabi A, Ekrami A, et al. Crack initiation and kinking behaviours of spot welded coach peel specimens under cyclic loading. Science and Technology of Welding and Joining. 2007;12(8):696-702, https://doi.org/10.1179/174329307X238416

32. BS EN ISO 14273:2001: Specimen dimensions and procedure for shear testing resistance spot, seam and .embossed projection welds 2002

33. Q. Yin CS, K. Isik, A.E. Tekkaya. A grooved in-plane torsion test for the investigation of shear fracture in sheet materials. International Journal of Solids and Structures. 2015; 66, 121-132. Article 8735. .https://doi.org/10.1016/j.ijsolstr.2015.03.032

34. C. Soyarslan MMG, A.E. Tekkay. A combined experimental–numerical investigation of ductile fracture in bending of a class of ferritic–martensitic steel. International (13), 1608-1626. 49Journal of Solids and Structures. 2012; https://doi.org/10.1016/j.ijsolstr.2012.03.009

35. Sylvain DANCETTE VM-J, Damien FABRÈGUE, Jacques MERLIN, Thomas DUPUY and Merlin BOUZEKRI. HAZ Microstructures and Local Mechanical Properties of High Strength Steels Resistance Spot Welds. ISIJ International,. 2011, 51(1):99-107, https://doi.org/10.2355/isijinternational.51.99

36. Lamouroux EHJ, Coutellier, Daniel, editor Detailed model of spot-welded joints to simulate the dynamical failure of car assemblies in Industrial Simulation; Dellft: 5th International Industrial Simulation Conference 2007, ISC .2007

37. Nielsen KL, Tvergaard, Viggo. Ductile shear failure or plug failure of spot welds modelled by modified Gurson ; 77(7):1031-.model. Engineering Fracture Mechanics. 2010 1047, https://doi.org/10.1016/j.engfracmech.2010.02.031

.38. Correlated Solutions Inc VIC 2D/3D Software. 2009

39. E92−17 A. Standard Test Methods for Vickers Hardness .and Knoop Hardness of Metallic Materials. 2017

40. Abdalla A, Hashimoto T, Neto CM, et al. Relationship between microstructure, mechanical properties and dislocation substructures in a multiphase steel. Revista Brasileira de Aplicações de Vácuo. 2008;23(2):52-57, https://doi.org/10.17563/rbav.v23i2.136

41. Chabok A, Galinmoghaddam E, De Hosson JTM, et al. Micromechanical evaluation of DP1000-GI dual-phase high-strength steel resistance spot weld. Journal of materials science. 2019;54(2):1703-1715, https://doi.org/10.1007/s10853-018-2886-z

42. Ramazani A, Mukherjee K, Abdurakhmanov A, et al. Characterization of Microstructure and Mechanical Properties of Resistance Spot Welded DP600 Steel. Metals. 2015;5(3):1704-1716, https://doi.org/10.3390/met5031704

43. Chabok A, Van der Aa E, De Hosson JTM, et al. Mechanical behavior and failure mechanism of resistance spot welded DP1000 dual phase steel. Materials & Design. 2017;124:171-182, https://doi.org/10.1016/j.matdes.2017.03.070

44. He Y, Rao Q, Tan Y. Investigation on the morphology of martensite in carbon steels. Journal of Central South University of Technology. 1996;3(2):122-134, https://doi.org/10.1007/BF02652191

45. Çalik A. Effect of cooling rate on hardness and microstructure of AISI 1020, AISI 1040 and AISI 1060 Steels. International Journal of Physical Sciences. .2009;4(9):514-518

46. Zhang H, Wei Z, Xie F, et al. Assessment of the Properties of AISI 410 Martensitic Stainless Steel by an Eddy Current Method. Materials. 2019;12(8):1290, https://doi.org/10.3390/ma12081290

47. Wei Y, Li Y, Zhu L, et al. Evading the strength–ductility trade-off dilemma in steel through gradient hierarchical .nanotwins. Nature communications. 2014;5(1):1-8

https://doi.org/10.1038/ncomms4580

48. Pavlina E, Van Tyne C. Correlation of yield strength and tensile strength with hardness for steels. Journal of materials .engineering and performance. 2008;17(6):888-893

https://doi.org/10.1007/s11665-008-9225-5

49. Zhang X, Yao F, Ren Z, et al. Effect of welding current on weld formation, microstructure, and mechanical properties in resistance spot welding of CR590T/340Y galvanized dual .phase steel. Materials. 2018;11(11):2310

https://doi.org/10.3390/ma11112310

50. Chao YJ. Ultimate strength and failure mechanism of resistance spot weld subjected to tensile, shear, or combined tensile/shear loads. J Eng Mater Technol. 2003;125(2):125- https://doi.org/10.1115/1.1555648.132

51. Liu C, Zheng X, He H, et al. Effect of work hardening on mechanical behavior of resistance spot welding joint during .tension shear test. Materials & Design. 2016;100:188-197

.1016/j.matdes.2016.03.12010https://doi.org/

52. Pouranvari M. Effect of resistance spot welding parameters on the HAZ softening of DP980 ferrite-martensite dual phase steel welds. World Applied Sciences Journal. .2011;15(10):1454-1458

53. Pouranvari M. Fracture toughness of martensitic stainless steel resistance spot welds. Materials Science and .Engineering: A. 2017;680:97-107

https://doi.org/10.1016/j.msea.2016.10.088

54. Furusako S, Murayama G, Oikawa H, et al. Current problems and the answer techniques in welding technique of auto bodies (first part). Nippon Steel Technical Report. .2013;103:69-75

55. Yates J, Zanganeh M, Tai Y. Quantifying crack tip displacement fields with DIC. Engineering Fracture .Mechanics. 2010;77(11):2063-2076

http://dx.doi.org/10.1016/j.engfracmech.2010.03.025